Energy & Environmental Science

This article can be cited before page numbers have been issued, to do this please use: S. Xu, Z. Chen, W. Zhao, W. Ren, C. Hou, J. Liu, W. Wang, C. Yin, X. Tan, X. Lou, X. Yao, Z. Gao, H. Liu, L. Wang, Z. Yin, B. Qiu, B. Hu, T. Li, C. Dong, F. Pan and M. Zhang, *Energy Environ. Sci.*, 2024, DOI: 10.1039/D3EE04199A.

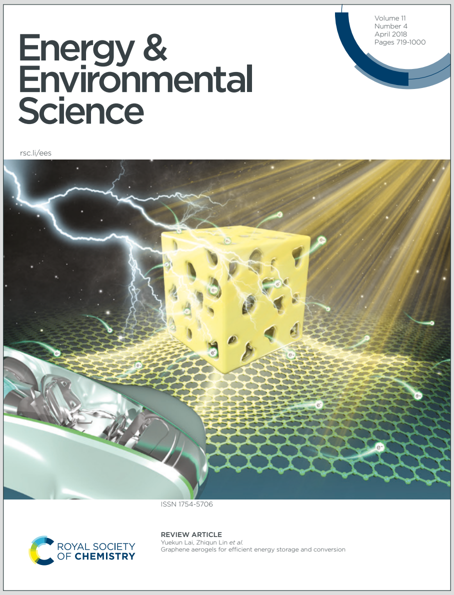

Volume 11
Number 4
April 2018
Pages 719-1000

Energy & Environmental Science

rsc.li/ees

ISSN 1754-5706

ROYAL SOCIETY OF CHEMISTRY

REVIEW ARTICLE
Yuekun Lai, Zhiqun Lin *et al.*
Graphene aerogels for efficient energy storage and conversion

ROYAL SOCIETY OF CHEMISTRY

rsc.li/ees

View Article Online
DOI: 10.1039/D3EE04199A

Broader context statement

Li-rich Mn-based (LMR) cathode owns a highest practical capacity among all commercial cathodes, but its structural nature (complex or solid solution) is still under debate, due to the extreme structural similarity of two layered-phase components, monoclinic phase ($C2/m$) and rhombohedral phase (R-3m). Herein, we combined multiple advanced techniques to comprehensively study the structural changes during synthesis of LMR cathode from different aspects of elemental distribution, local structure, long-range structure, and short-range structure, revealing a clear process from the formation of two phases to the gradual phase fusion, eventually to a nearly solid solution. Particularly, X-ray pair distribution function (PDF) analysis combined with theoretical simulation reveal for the first time that the transition metal (TM)-TM distance increases with the progress of the phase fusion, which makes the short-range structural change in TM-TM atomic pair become an effective parameter for judging the extent of phase fusion. Eventually, excellent electrochemical performance was achieved in LMR through adjusting the phase fusion extent, and the strategy was further validated in another P2-O3 bi-phase complex cathode for Na-ion battery. This work represents a significant stride in cathode technology and methodology for analyzing complicated multi-phase systems.

View Article Online
DOI: 10.1039/D3EE04199A

Multi-Angle Tracking Synthetic Kinetics of Phase Evolution in Li-Rich Mn-Based Cathodes

Shenyang Xu[1], *Zhefeng Chen*[1], *Wenguang Zhao*[1], *Wenju Ren*[1,2], *Chenxin Hou*[1], *Jiajie Liu*[1], *Wu Wang*[3], *Chong Yin*[4], *Xinghua Tan*[1], *Xiaobing Lou*[5], *Xiangming Yao*[1], *Zhihai Gao*[1], *Hao Liu*[6], *Lu Wang*[1], *Zuwei Yin*[1], *Bao qiu*[7], *Bingwen Hu*[5]*, *Tianyi Li*[8], *, *Cheng Dong*[1], *Feng Pan*[1], *, *Mingjian Zhang*[9], *

[1] School of Advanced Materials, Shenzhen Graduate School, Peking University, Shenzhen 518055, China.

[2] School of Advanced Manufacturing Engineering, Chongqing University of Posts and Telecommunications, Chongqing 400065, China.

[3] Shenzhen Key Laboratory of Thermoelectric Materials, Department of Physics, Southern University of Science and Technology, Shenzhen 518055, China.

[4] Ningbo Ronbay Lithium Battery Material Co., Ltd, Ningbo 315400, China.

[5] Shanghai Key Laboratory of Magnetic Resonance, State Key Laboratory of Precision Spectroscopy, School of Physics and Electronic Science, East China Normal University, Shanghai 200241, China.

[6] Institute for Applied Materials, Karlsruhe Institute of Technology, Hermann-von-Helmholtz-Platz 1, Eggenstein-Leopoldshafen 76344, Germany

[7] Ningbo Institute of Materials Technology and Engineering, Chinese Academy of Sciences, Ningbo 315201, China

[8] Chemical Sciences and Engineering Division, Argonne National Laboratory, Lemont, IL 60439, USA.

[9] School of Science and Engineering, The Chinese University of Hong Kong, Shenzhen, Guangdong 518172, China.

View Article Online
DOI: 10.1039/D3EE04199A

*Corresponding author. E-mail: bwhu@phy.ecnu.edu.cn; tianyi.li@anl.gov; panfeng@pkusz.edu.cn; zhangmingjian@cuhk.edu.cn

View Article Online
DOI: 10.1039/D3EE04199A

Abstract

As the commercial cathode with the highest practical capacity, the structural nature of Li-rich Mn-based cathodes (LMR), composite or solid solution, is still under debate. Due to the extreme structure similarity of two layered-phase components, monoclinic phase ($C2/m$) and rhombohedral phase (R-$3m$), no single tool can resolve this concern alone. Herein, we combined multiple advanced techniques to comprehensively study the structural changes during synthesis of LMR cathode from different aspects of elemental distribution, local structure, long-range structure, and short-range structure, revealing a clear process from the formation of two phases to the gradual phase fusion, eventually to a nearly solid solution. Particularly, X-ray pair distribution function (PDF) analysis combined with theoretical simulation reveal for the first time that the transition metal (TM)-TM distance increases with the progress of the phase fusion, which makes the short-range structural change in TM-TM atomic pair become an effective parameter for judging the extent of phase fusion. Eventually, excellent electrochemical performance was achieved by balancing capacity and cycling stability through adjusting the phase fusion to a medium extent in lithium and sodium two layered-phase components. This study establishes an approach to investigate the structural evolution in the complicated multiple-phase system, and provides valuable insights into the design and optimization of cathodes by tuning the phase fusion extent.

Keywords: Synthetic kinetics, Li-rich layered oxide cathode, phase fusion, solid solution, short-range structure

DOI: 10.1039/D3EE04199A

Introduction

Li-rich Mn-based materials (LMR), written as $x\mathrm{Li[Li_{1/3}Mn_{2/3}]O_2}\cdot(1-x)\mathrm{LiTMO_2}$ (TM= Ni, Co, Mn), are one of the most promising candidates for next-generation cathodes with high energy density.[1-5] Nevertheless, the complicated elemental composition and phase structures of LMR, which involves four metal elements and diverse cation arrangements, pose substantial challenges in controlling the synthesis process and ensuring consistent electrochemical performance. Furthermore, there is a long-standing debate regarding LMR's phase structure. Some studies propose a composite made up of two layered phases $\mathrm{Li_2MnO_3}$ (S. G. *C*2/*m*) and $\mathrm{LiTMO_2}$ (S. G. *R*-3*m*),[6-11] while others suggest a solid solution of two phases. [12, 13] Actually, the real structure greatly depends on the synthetic conditions, and different temperatures, time, and heating/cooling rates would lead to different structures.[14] That is why there are so many different reports about the structure and electrochemistry of LMR cathodes. Therefore, it is essential and crucial to figure out the whole process of phase structure evolution during the synthesis of LMR cathodes, which can end up the long-standing controversy and benefit to the controllable and precise synthesis of so complicated material system.

Our recent study revealed that lattice strain of two phase of LMR is the origin of structural degradation.[15] Nevertheless, the two compositional phases in LMR are extremely similar, thus posing a great technique challenge. They have the same O3-type layered structure compositing with the alternately stacking Li layers and transition metal (TM) layers, and only show tiny differences in the elemental composition and cationic arrangement in TM layers. Element-sensitive transmission electron microscope (TEM) energy dispersive X-ray spectroscopy (EDX) can distinguish two layered phases with different TM compositions by probing the elemental distribution, but it fails if the difference in elemental spatial distribution is at the ten-nanometer level. [11, 14] X-ray diffraction (XRD) coupled with Rietveld refinement is another powerful technique to identify the long-range phase structure and analyze the phase composition, but it does not work well here since XRD patterns of two phases nearly overlap with each other except the superlattice peaks of monoclinic phase. Local-structure sensitive high-resolution TEM can probe the spatial distribution of two phases, but it works only when taking images along the special direction showing the Li-Mn-Mn…Li-Mn-Mn… arrangement in TM layers, which is the sole structure feature of monoclinic phase different from rhombohedral phase. X-ray total diffraction coupling with pair distribution function (PDF) analysis has the unique capability of analyzing both long-range and short-range structure information, especially the later part may work to distinguish so similar two phases with tiny local structural differences.[6, 12, 13] Overall,

View Article Online
DOI: 10.1039/D3EE04199A

no single available technique can adequately track the whole phase transition process from the two-phase composite to the solid solution phase since the respective detection limits in element and structure.[16-18] In this context, it is required to combine various advanced techniques together for gaining a comprehensive understanding of the structure evolution behavior in LMR cathode materials.

Herein, we perform a systemic investigation of the phase transition during the sol-gel synthesis of LMR cathodes using a combination of advanced techniques, including TEM EDX, transmission Kikuchi diffraction (TKD), TEM, synchrotron X-ray diffraction (SXRD), PDF analysis, solid-state nuclear magnetic resonance spectroscopy (ssNMR) and theoretical calculations, from multiple aspects of elemental distribution, long-range structure, local structure, and short-range atomic ordering (**Scheme 1**). The whole process is clearly elucidated from the formation of two phases to the gradual phase fusion, eventually to a complete phase fusion. Especially, PDF analysis provides a clear change in the distance of the TM-TM atomic pair with the temperature, which can act as an important judgement to track the extent of two-phase fusion. Furthermore, LMR cathode with a medium extent of phase fusion exhibits the excellent cycling stability without sacrificing the capacity due to the unique nanodomain structure. These studies enhance our understanding of the structural nature of LMR cathode and provide the possibility to harness full potential of LMR cathodes in practical applications.

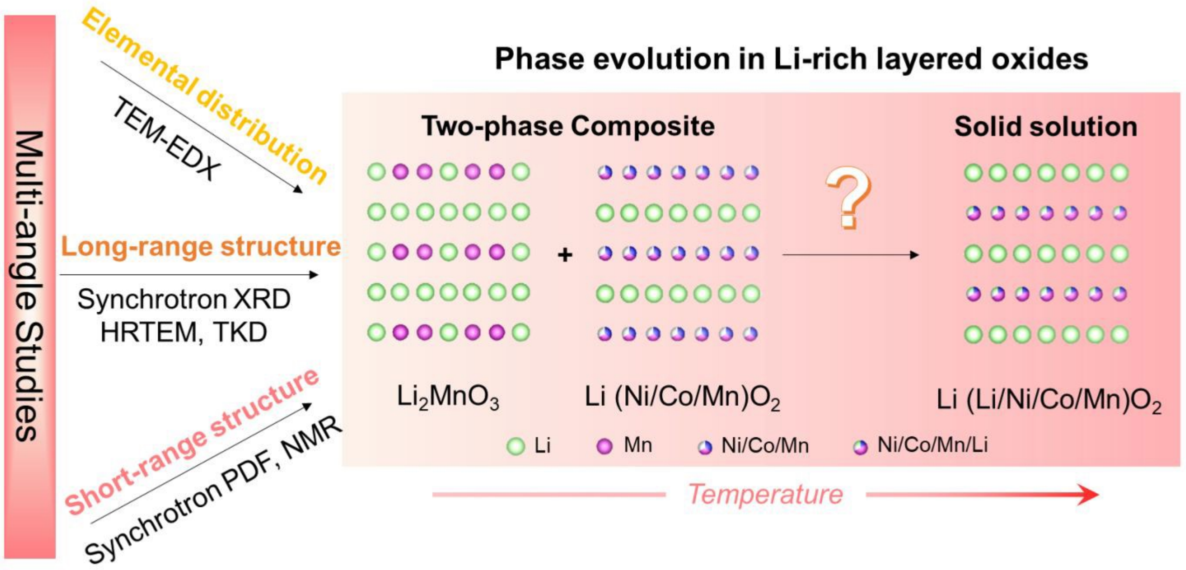

Scheme 1. Schematic illustration of a combination of advanced tools to study the phase structure evolution of LMR cathode from multiple angles.

View Article Online
DOI: 10.1039/D3EE04199A

Results and Discussion

The change in elemental distribution and local phase structure

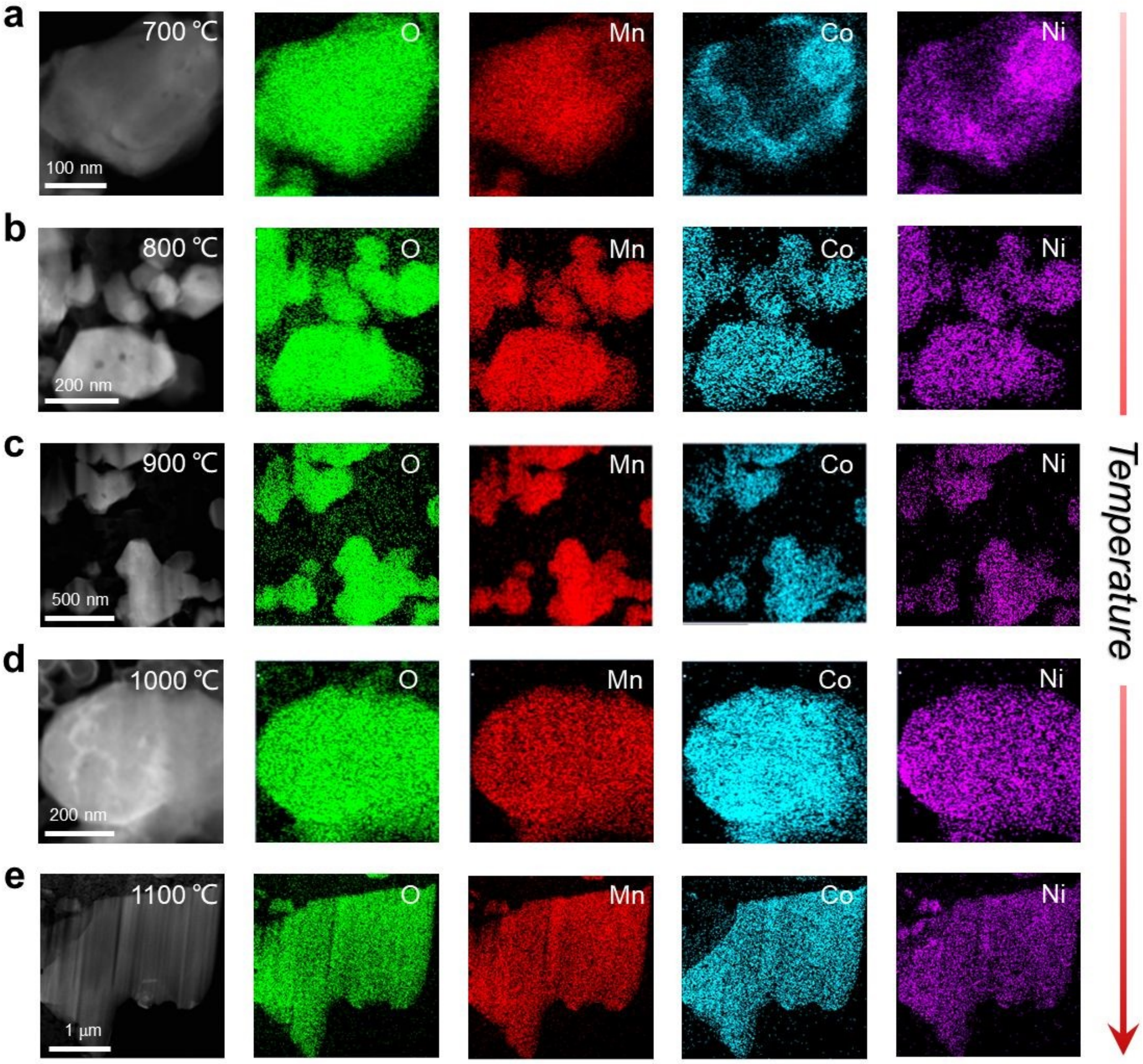

Figure 1. Elemental interdiffusion kinetics. *Ex-situ* TEM images and the corresponding EDX spectra of O, Mn, Co, and Ni for LLNCM-700 (a), LLNCM-800 (b), LLNCM-900 (c), LLNCM-1000 (d) and LLNCM-1100 (e).

Since the formation and interplay of two layered phases accompany with the TM segregation and interdiffusion during the synthesis of LLNCM, we adopted TEM EDX to track the change in elemental distribution with the temperature (**Fig. 1**). As for LLNCM-700 (Fig. 1a and Fig. S3), the elemental distribution of Mn, Co, Ni is not uniform among the primary particles, showing the Mn-concentrated particles and the Co/Ni-concentrated particles (nealy a core shell structure). It should correspond to the formation and separation of two layered phases

View Article Online
DOI: 10.1039/D3EE04199A

Li_2MnO_3 (Mn-rich) and $LiNi_{1/3}Co_{1/3}Mn_{1/3}O_2$ (NCM111, Ni/Co rich) in LMR cathode, since Li_2MnO_3 can be obtained at a lower temperature than NMC111 (Fig. S4).[19-21] When the temperature reaches 800 ^oC and above (Fig. 1b-e), the Mn, Co and Ni distribution becomes uniform at the nanoscale. It indicates that the elemental interdiffusion of Mn, Co and Ni between Li_2MnO_3 particles and NCM111 particles takes place during the further sintering process, and is basically completed by 800 ℃. It roots in the structural similarity of two phases, and confirms the element tolerance of 3*a* (TM) sites in NCM111 and the 4*g* (Mn) sites in Li_2MnO_3. The results also tell us that TEM EDX fails to track the further phase fusion process above 800 ℃.

To track the phase evolution above 800 ℃, HRTEM images are taken at the particle surface and in the bulk of different samples. As shown in Fig. 2a-c and Fig. S5, it is easy to find the phase fusion regions with the clear grain boundary within the individual particles of LLNCM-800, LLNCM-900, and LLNCM-1000. They all present two layered phase domains (Region 1 and 3 marked in Fig. 2a-c) and the spinel-like region in between (Region 2 marked in Fig. 2a-c). It is hard to identify two layered phase regions as monoclinic phase or rhombohedral phase due to the same O3-type arrangement and the similar inter-layer distances. The spinel-like region in between hints that the phase fusion between two layered phases progresses through the TM migration and re-arrangement. When the temperature reaches to 1100 ℃, we can not find any grain boundary within single particles. As shown in Fig. 2d, the same layered lattice fringes with the same orientation can be observed in the bulk region (Region 1) and at the particle surface (Region 2). Furthermore, we expand upon the discussion regarding bulk structure of LLNCM-1000 and LLNCM-1100 by high-angle annular dark field-scanning transmission electron microscopy images (HADDF-STEM). As depicted in Fig. S6, LLNCM-1100 exhibits distinct particles. This observation substantiates the conclusion that the grain boundaries within LLNCM-1100 are inter-particle. In Fig. 2e-f, both LLNCM-1000 and LLNCM-1100 exhibit no obvious contrast difference in transition metal layers. Nevertheless, the intensity profile of LLNCM-1000 displays a greater variance in brightness, hinting a more random arrangement of transition metals in LLNCM-1100. This hypothesis warrants further investigation through analysis of local structural change. The selected area electron diffraction (SAED) is further performed to check the structure at the single particle level. As shown in Fig. S7, it exhibit different crystalline directions, demonstrating the polycrystalline character for LLNCM-1000 particle. While the LLNCM-1100 particle demonstrates a singular orientation (Fig. S8), confirming the single crystal character. These findings are in alignment with the

View Article Online
DOI: 10.1039/D3EE04199A

outcomes obtained from TKD analysis (Fig. 2g-i). The TKD tests with the unique capablity to identify the crystal orientation of the nanocrystals with a sub-10 nm spatial resolution,[22] were performed on the individual particles of LLNCM-1000 and LLNCM-1000 (Fig. 2g). As shown in Fig. 2h, the projection maps from three different angles for LLNCM-1000 show the separation of two diffraction spots (marked by the arrows). It indicates that there are different cystal orientations within single particle, hinting the polycrystal or twin-crystal nature. Differently, the projection maps from three different angles for LLNCM-1100 (Fig. 2i) only show one diffraction spot, hinting the single-crystal nature of the individual particle. In brief, HRTEM combined with TDK results can tell us that it achieves relatively high degree of fusion at the nanodomain scale by 1100 °C, but can not distinguish the different extent of phase fusion from 800 to 1000 °C.

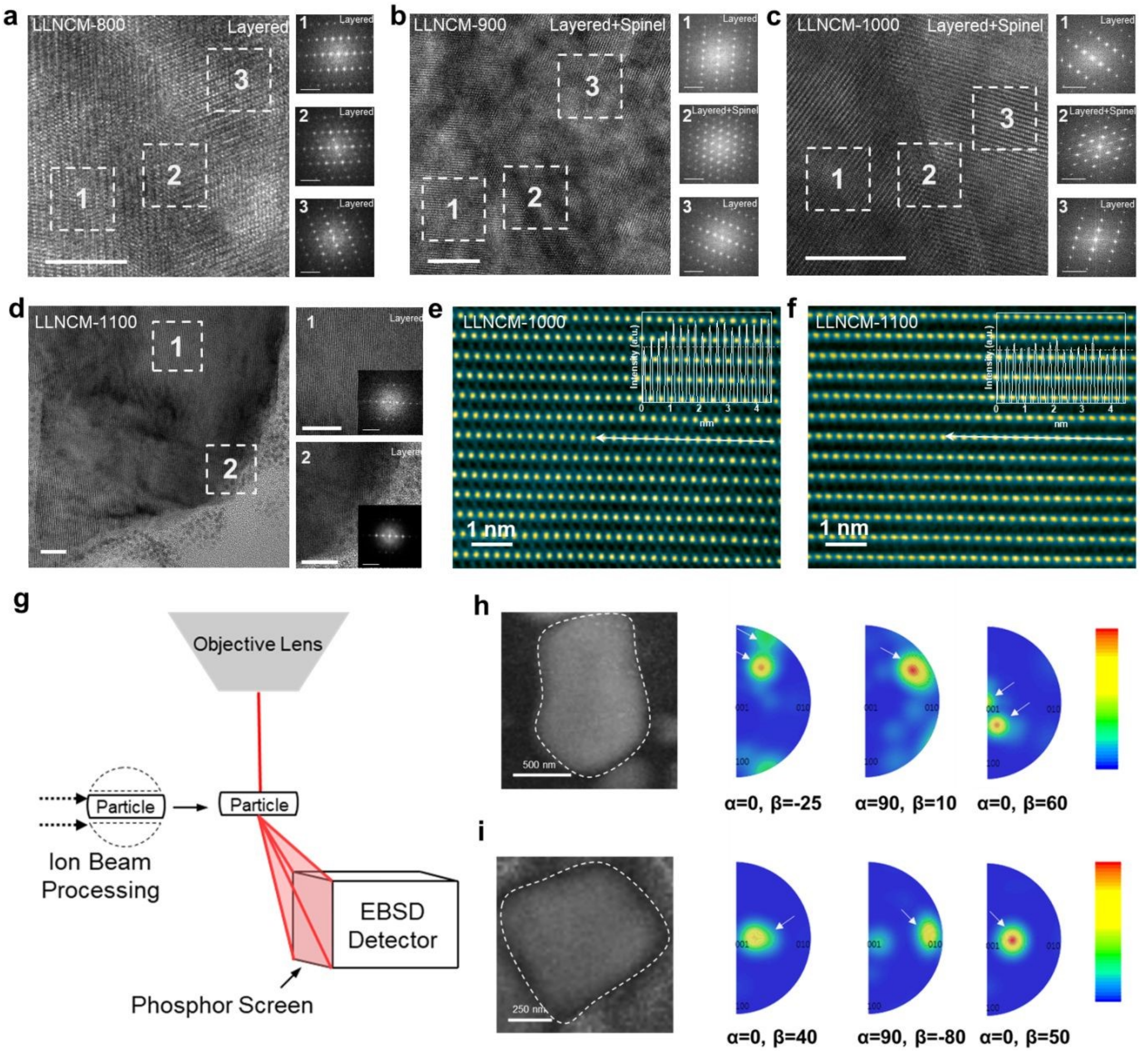

Figure 2. Microstructure changes with the temperature. HRTEM images of LLNCM-800 (a), LLNCM-900 (b), LLNCM-1000 (c) in the bulk and LLNCM-1100 (d). The FFT maps are

deduced from the corresponding regions. The scale bars in HRTEM images and FFT maps are 10 nm and 2 1/nm, respectively. (e-f) HADDF-STEM images of LLNCM-1000 and LLNCM-1100. (g) Schematic diagram of TKD test on the cross-section sample of the individual particle. Inverse pole figures (IPF) and corresponding images of LLNCM-1000 paticle (h) and LLNCM-1100 particle (i).

The change in long-range structure

Li_2MnO_3 and NCM111 have the same O3-type layered structure compositing with the alternately-stacking Li layers and transition metal (TM) layers, and only show tiny differences in the elemental composition and cationic arrangement in TM layers. As shown in Fig 3a, TM layers in monoclinic Li_2MnO_3 consist of MnO_6 octahedra interleaved with LiO_6 octahedra. TM layers in rhombohedral $LiTMO_2$ are made up of disordered NiO_6, CoO_6 and MnO_6 octahedra. The simulated XRD patterns of Li_2MnO_3 and $LiTMO_2$ are shown in Fig. S9-S10. All diffraction peaks of $LiTMO_2$ are basically overlapped with those of Li_2MnO_3. As a powerful tool to identify the phase structure of crystalline materials, SXRD was applied to investigate the phase evolution during the sintering process.[23] Fig. 3b show the SXRD patterns of LLNCM-700, LLNCM-800, LLNCM-900, LLNCM-1000, and LLNCM-1100. It is clear, $(003)_R$ and $(104)_R$ peaks of the rhombohedral phase NCM111 are nearly overlapped with $(001)_M$ and $(131)_M$ peaks of the monoclinic phase Li_2MnO_3, respectively, due to the very close crystal plane spacings with the difference ~0.01 Å ($d(003)_R$ = 4.7423 Å, $d(104)_R$ = 2.0326 Å, $d(001)_M$ = 4.7350 Å, $d(131)_M$ = 2.0234 Å) (Fig. 3a).

Nevertheless, we can distinguish the two phases a little according to the asymmetric peak shape and the peak shift of the enlarged prominent peaks in Fig. 3c. The $(003)_R/(001)_M$ peak shows a continuous peak shift to the large *d*-spacing direction with temperature (marked by the arrow in Fig. 3c), corresponding to the increase of inter-layer distance. It hints a phase fusion process from the monoclinic phase to the rhombohedral phase since the rhombohedral phase has a larger interlayer distance than the monoclinic phase. It is consistent with TEM images in Fig. 1, evidencing progressive phase fusion from the nanoparticle composite to the nanodomain-level interdiffusion.

In addition, it is reasonable that the extent of peak overlapping should increase with the gradual two-phase fusion, leading to the decrease of the full widths at half maximum (FWHM). Therefore, the FWHM values (Fig. 3d) were plotted as a function of temperature to track the two-phase fusion. The FWHM values of both peaks show the decrease trend with the temperature from 700 °C to 900 °C, hinting the phase fusion to some extent, since they have similar particle sizes (Fig. S1-S2, Fig. S11). Especially, there are big drops from 700 °C to 800 °C, which corresponds to the change of elemental distribution from the non-uniformity to uniformity at the nanoscale level (Fig. 1a-b). It demonstrates a corresponding correlation between phase fusion and elemental diffusion. When the temperature further increases, the changes of the FWHM values above 900 ℃ are not obvious, hinting the parameter FWHM hardly reflects the higher extent of phase fusion above 900 ℃. And the *in-situ* heating XRD analysis were performed at 800, 900 and 1000 ℃ (Fig. S12-S15). The results demonstrated that temperature exerted a stronger influence over structural changes of lithium-rich materials than the prolonged heating duration (> 5 hours), and the cooling process had minimal effect on the FWHM values. Thus, the capability of X-ray diffraction to discern the nuances of the fusion process at the particle level warrants further investigation.

Rietveld refinement was also performed on *ex-situ* SXRD patterns to try to analyze the change in phase composition (Fig. S16-S17 and Table S2-S4). As shown in Fig. S17 and Table S3-S4, good fitting results with the similar Rwp values can be obtained even using different phase compositions at 1000 ℃. It indicates that Rietveld refinement loses efficacy to track the phase composition when two phases exhibit extremely similar structures. Refinements were further performed using stacking fault models (Figure S18). [24-26] As the temperature increases, the staking fault probability basically shows a decrease trend (Table S5). It is reasonable that the higher phase fusion degree at high temperatures would break up the Li/Mn ordering in the transition metal layer, leading to the less stacking faults. The increasing temperature will bring with the more well-defined atomic arrangement. As a result, the diffraction peaks appear sharper.

Given the challenges associated with employing traditional XRD analysis to monitor fusion at the nanodomain scale, it is imperative to peform specialized experiments aimed at elucidating the fusion process within LLNCM-900, LLNCM-1000, and LLNCM-1100. We decoupling the fusion process by using the same proportion of NCM111 and Li_2MnO_3 materials as the experimental materials, dispersed the cathode of the two-phase structures on both sides to prevent the phase fusion, and conducted XRD testing after adopting the same calcination conditions (illustrated in the inset of Fig. 3e and Fig. S19). Then we strictly designed XRD experiments to exclude the influences of crystallinity and particle size on the FWHM of main peaks (Fig. S20). According to Scherrer's formula:

View Article Online
DOI: 10.1039/D3EE04199A

$$FWHM = \frac{k\,\lambda}{D_{hkl}Cos\theta_{hkl}}$$

D_{hkl} is grain size in normal direction, k is the shape factor, λ is the wavelength, we calculated the effect of grain size differences on the FWHM of the $(003)_R/(001)_M$ peak (Fig S20), and found that when the grain sizes differed by 100 nm, the difference in half-peak width of XRD measured under the copper target was less than 0.015 degrees. It is clear that the difference in FWHM value at 900 ^oC (>0.03 degrees) is much larger than the error (0.015 degrees, resulted from the effect of grain size on FWHM mentioned above). Accordingly, the difference in FMHW at 900 ^oC can be used as a criterion for nanodomain diffusion. But when the temperature rises to 1000 ^oC or beyond, no nanodomain scale diffusion occur, local structures need to be used for judgment.

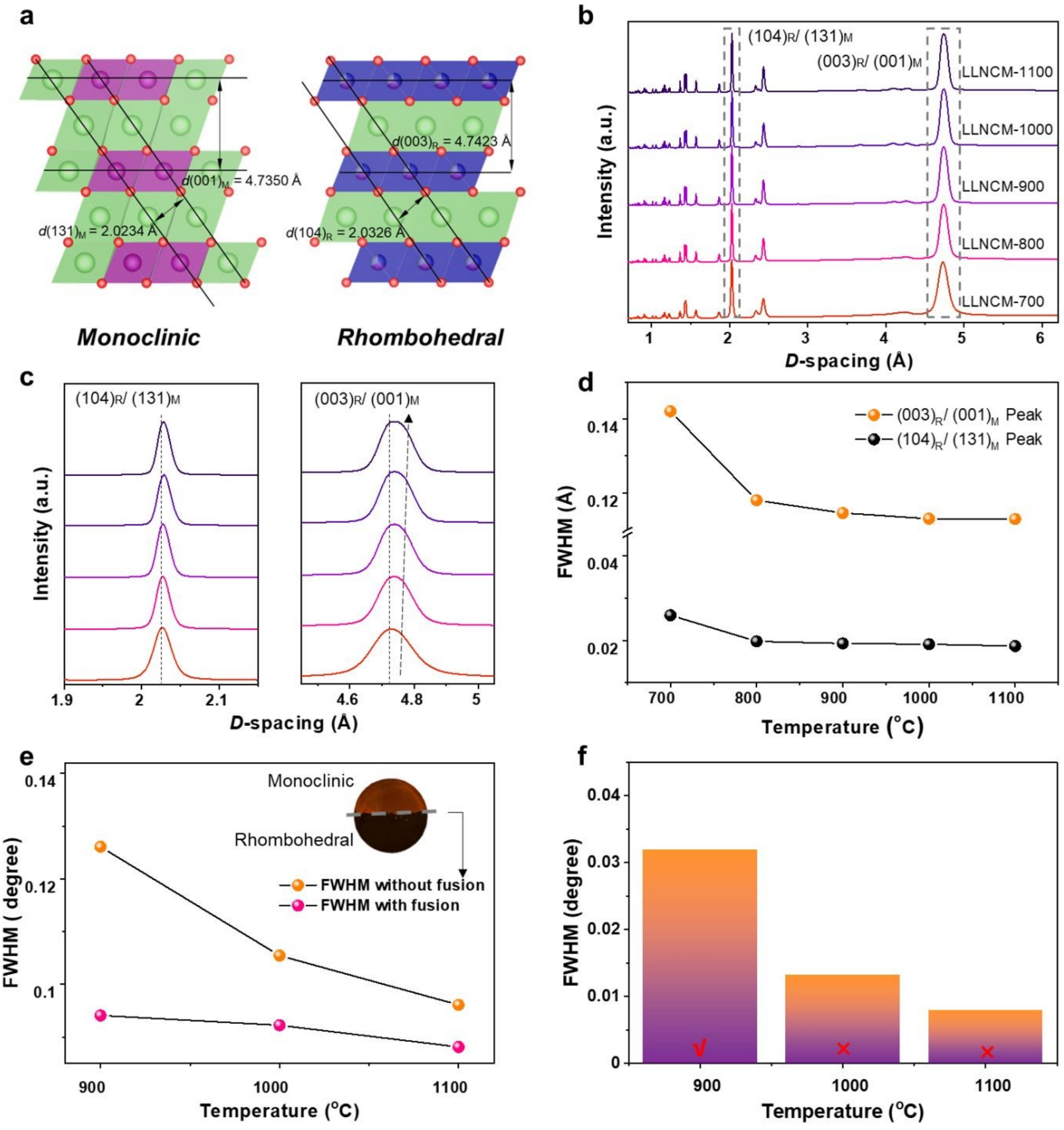

View Article Online
DOI: 10.1039/D3EE04199A

Figure 3. Long-range structure evolution. (a) The crystal structures of monoclinc phase and rhombohedral phase with the corresponding crystallographic planes marked. (b) *Ex-situ* SXRD patterns of as-prepared Li-rich Mn-based layered oxides LLNCM-700, LLNCM-800, LLNCM-900, LLNCM-1000 and LLNCM-1100. (c) The enlarged $(003)_R/(001)_M$ and $(104)_R/(131)_M$ peaks from (b). (d) The corresponding FWHM values of $(003)_R/(001)_M$ and $(104)_R/(131)_M$ peaks as a function of temperature. (e) $(003)_R/(001)_M$ FWHM values with and without two-phase diffusion at different temperatures and (f) the corresponding differences in FWHM from (e).

Overall, synchrotron XRD, is able to track the beginning part of two-phase fusion from the nanoparticle composite to the initial phase fusion within a single particle at nanodomain scale, but works not so well to probe the higher extent of phase fusion with the TM interdiffusion at the atomic level in individual particles.

The change in short-range structure

Based on the results above, the phase fusion above 900 ℃ is hard to detect since this part only involves Li/TM diffusion and rearrangement in TM layers at the atomic level without changing lattice parameters much. Here synchrotron X-ray total scattering coupling with PDF analysis was employed to detect the short-range structural changes, especially the changes of TM coordination environments accompanied with the TM rearrangement. As shown in Fig. S21, the full PDF patterns of five samples present very similar profiles, hinting the similar long-range layered structures. To further examine the short-range structure change, the region in 1.5-3.2 Å is enlarged in Fig.4a. The peaks around 1.9 and 2.8 Å can be assigned to TM-O bond and TM-TM atomic pair, respectively. All samples have nearly the same TM-O peak position, indicating that TM-O bond length in TMO_6 octahedra does not change with the phase fusion. The TM-TM peak gradually shifts to the high *r* direction with temperature, especially for LLNCM-1100, indicating a longer average TM-TM distance at 1100 °C (Fig.4b). The refinement results of PDF patterns are summarized in Fig. S22 and Table S6-S7. We found that this changes in the TM-TM peak intensity and position were mainly due to the variations of lattice parameters and oxygen positions. To further investigate the changes in the valence state of TM and the local structure, X-ray absorption near edge structure (XANES) and extended X-ray absorption fine structure (EXAFS) spectra were collected on both LLNCM-1000 and LLNCM-1100. As shown in Fig. S23, Mn exhibits a decrease in the valence state with temperature, while Ni and Co exhibits increase in the valence state. This suggests a higher

View Article Online
DOI: 10.1039/D3EE04199A

degree of Ni and Co incorporation into the Li@Mn_6 structure.[27-29] The EXAFS spectra for Ni *K*-edge and Co *K*-edge exhibit elongated TM-TM distances and diminished intensity for Ni-TM and Co-TM interactions (Fig. S24).

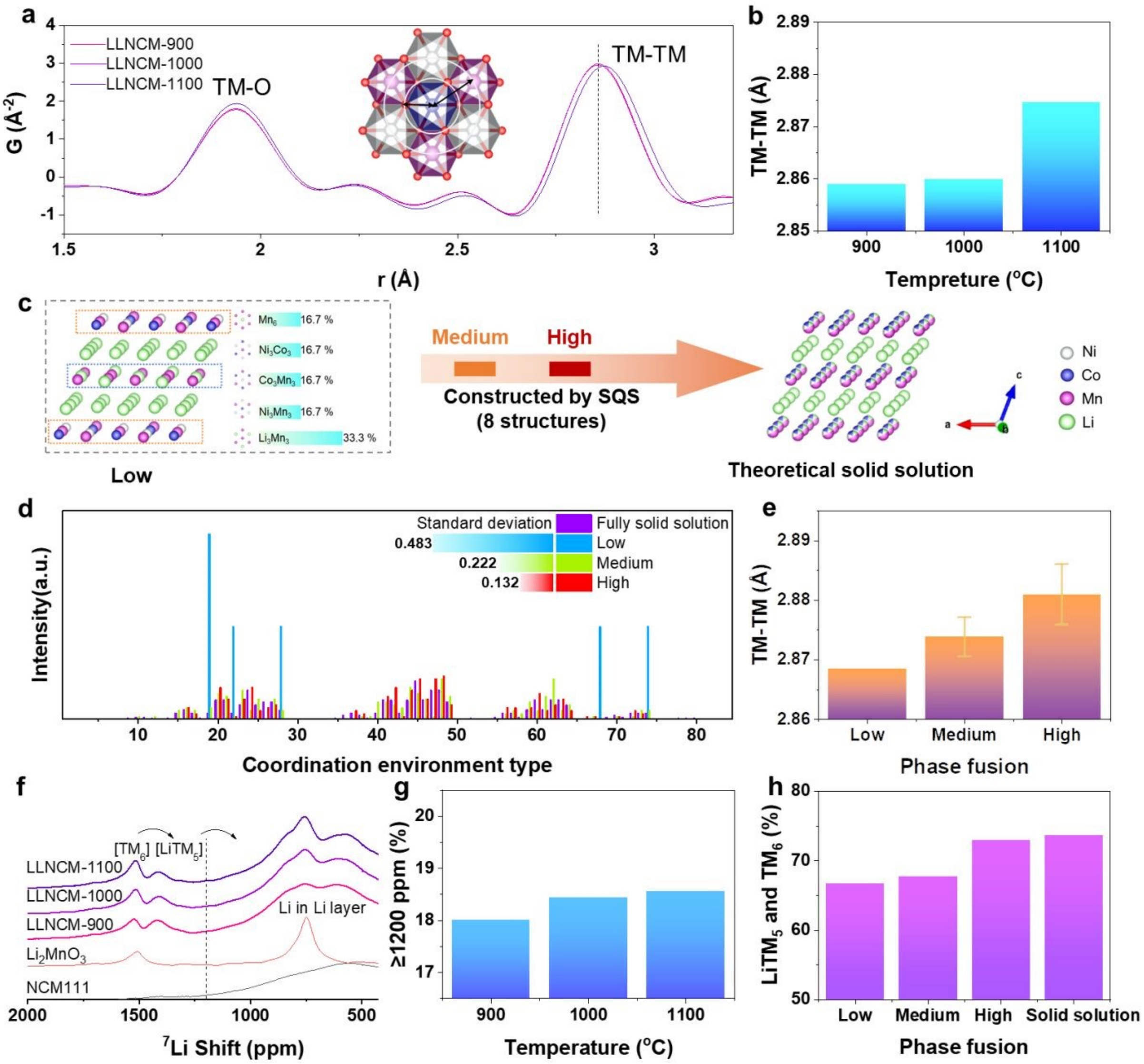

Figure 4. The short-range structure evolution at the atomic scale. (a) Synchrotron PDF patterns of LLNCM-900, LLNCM-1000 and LLNCM-1100 in the short *r* region of 1.5-3.2 Å. (b)The TM-TM distance as a function of temperature, deduced from (a). (c) Schematic illustration to show the construction of structure models with the low, medium, and high extents of phase fusion between Li_2MnO_3 and NCM111 phases by SQS method. SQS means special quasi-random structure. The structure models with medium and high phase fusion extents were presented in Fig. S18-S19. (d) The local coordination environment statistics in structure models with the low, medium, and high extent of phase fusion. The detailed results are summarized in Table S8-S10. (e) The calculated TM-TM distance as a function of the extent of phase fusion.

View Article Online
DOI: 10.1039/D3EE04199A

(f) Deconvoluted ^{7}Li MAS NMR of LLNCM-900, LLNCM-1000, LLNCM-1100, NCM111 and Li_2MnO_3. (g) The area proportions of resonances ≥1200 ppm for LLNCM-900, LLNCM-1000 and LLNCM-1100. . (h) Proportions of $LiTM_5$ and TM_6 configurations in transition metal layers as a function of the phase fusion extent based on the model structures.

The elongation of TM-TM distance may be related to the phase fusion process. In order to validate the deduction, we developed a special quasi-random structure (SQS) system to construct structure models with different fusion degrees - low, medium and high (Fig. 4c and Fig. S25-26). The low fusion model (initial structure) is composited with alternately stacked TM layers from Li_2MnO_3 (marked by blue dashed rectangle) and TM layers from NCM111 (marked by orange dashed rectangle). In the solid solution structure with the maximum degree of phase fusion, Li^+ and the transition metal ions are randomly arranged in TM layers. The system energy increases with the degree of phase fusion (Fig. S27). This aligns with the generally accepted principle that greater fusion requires higher energy input. Within these structure models, different coordination environments of Li in TM layers are numbered and counted, and presented in the histogram form (Fig. 4d). The standard deviations were calculated using the fully solid solution as the reference, and the values are 0.483, 0.222 and 0.132 for low, medium and high degree of phase fusion, which is self-consistent and reasonable. We further extracted the TM-TM distances from these structure models and found that a positive correlation between TM-TM distance and the phase fusion degree (Fig. 4e), which is highly consistent with the experimental results (Fig. 4b). We can deduce that the change in TM-TM distance arises from the variations in local coordination environments. Combining the PDF results and theoretical calculations, we can conclude that the TM-TM distance can act as an effective parameter to quantify the extent of phase fusion when the samples have identical elemental compositions and are synthesized using the same methodology. The larger TM-TM distance indicates the higher extent of phase fusion. The TM-TM distance of LLNCM-1100 obtained from PDF results is 2.875 Å (Fig. 4b), close to the calculated value (2.88 Å) for the high fusion extent (Fig. 4e). So LLNCM-1100 can be considered to approach the ideal solid solution.

To further confirm the realiablity of theoretical calculations, we examined the changes in Li local environment with temperature by ^{7}Li magic angle spin (MAS) ssNMR. The resonances >1200 ppm in Fig. 4f can be attributed to Li ions in TM layers, possessing mainly Li_1TM_5 and TM_6 local structures, respectively. [30-34] The resonances below 1200 ppm should be mainly assigned to Li in Li layers and TM layers , but the high ppm region shows a different

View Article Online
DOI: 10.1039/D3EE04199A

contribution from Li in Li layer in Li_2MnO_3 and NCM111. To quantify Li contents in TM layers, we calculated the area of resonances ≥ 1200 ppm, and deduced the proportion in the whole range of 450-2000 ppm. As shown in Fig. 4g, the proportion increases with temperature. It may be correlated with the phase fusion. Correspondingly, we counted Li local structures containing 5 TM and 6 TM from these calculated structure models, and plotted the number as the phase fusion extent in Fig. 4h. It is clear that the proportion shows an increase trend with the phase fusion extent. It means that the higher phase fusion extent will brings with more Li local structures with TM_5 and TM_6, which is consistent with the ssNMR results in Fig. 4g.

Overall, the consistency between PDF results, ssNMR data and theoretical calculations provides irrefutable support for the higher phase fusion with temperature.

Understanding of phase fusion

The comprehensive experimental and theoretical results above can allow us to depict the whole process of two-phase fusion in the complicated LMR system from multiple angles in detail. As shown in Fig. 5a, the whole process can be divided into three stages: (1) the formation of two phases; (2) Composite of two phases at the nanodomain scale; (3) high-extent fusion of two phases at the atomic level. At the 1st stage, Li_2MnO_3 phase and NCM111 phase formed into nearly core-shell particles at around 700 ℃, which can be determined by the TM segregation detected by TEM EDX and the phase compositions detected by SXRD. At the 2nd stage, two phases merge at the nanodomain scale above 800 ℃, confirmed by the uniform elemental distribution by TEM EDX, the phase boundaries observed in HRTEM images of LNCM-800, LLNCM-900, and LLNCM-1000, the decreased FWHM values and peak shift of the main peaks in SXRD patterns. At the last stage, phase fusion comes to a higher extent and proceed among the different phase nanodomains, mainly through the TM migration and rearrangement in the TM layers of two layered phases, eventually to a nearly solid solution at 1100 ℃, which can be evidenced by the peak shift of TM-TM peak in PDF patterns from 1000 to 1100 °C, the changes in Li coordination environments observed in ssNMR, as well as the disappearance of grain boundaries in HRTEM images and TKD tests.

In the whole process of phase fusion, O coordination environment could change with the phase fusion extent, which may affect the electrochemistry a lot. [35] To validate this deduction, the electrochemical performance of five samples was evaluated in half coin cells. The initial charge/discharge curves are compared in Fig 5b. The plateau above 4.45 V comes from lattice oxygen oxidation.[36] It is clear, the plateau becomes shorter with the temperature, indicating that

View Article Online
DOI: 10.1039/D3EE04199A

the contribution of oxygen redox to the capacity decreases with the phase fusion extent, which is further confirmed by the quantitative analysis and eliminating experimental method factors (Fig. S28-S29). When the phase fusion extent reached the maximum at 1100 ℃, the O redox activity is sharply suppressed, indicated by the big capacity drop from 1000 to 1100 ℃, which can be attributed to the dispersion of Li@Mn_6 superstructural units.[14, 37, 38] Fig. S30 illustrates that the band gap in the total density of states (DOS) narrows from 1.72 eV to 0.72 eV upon increasing the phase fusion degree. This reduction suggests an enhancement in electrical conductivity and potentially improved cycling performance.[39] Furthermore, the oxygen PDOS shows a notable decrease in band gap, indicating the oxygen is easier to be oxidized (Fig. S31). Synchronous thermal analyzer (TG-DSC) and Phase diagram experiments were further performed to confirm the fusion ability of 1100 ^{o}C, demonstrating that interparticle elemental diffusion was achieved (Fig. S32-S33). This is significant because Li_2MnO_3 has traditionally been regarded as oxygen inert. However, upon sealing and sintering a tube of the material at 1100 °C for 1 hour, reversible oxygen activity was observed (Fig. S33c). The results indicate sintering at 1100 ℃ could affect the local structure and thus the oxygen redox chemistry. Therefore, the judgment of the phase fusion degree is valid above 900 ^{o}C. Multi-angle tracking oxygen behavior of phase evolution is needed to further understand the oxidation mechanism. [40-43]The long-cycling results show that the sample with the medium level of phase fusion has better electrochemical and structural stability and smaller voltage decay (Fig. 5c, Fig. S34 and Fig. S35), which is consistent with our previous work.[14, 37] Overall, LLNCM-1000 exhibits the best electrochemistry due to its balanced capacity and stability performance. Therefore, it is feasible to adjust the degree of phase fusion to achieve good cycling stability without sacrificing much O redox activity.

This direct correlation between phase fusion and temperature enables innovative approaches to designing new materials. We further applied this phase fusion control strategy to another Na-ion battery cathode composited with two layered phases (*C*2/*m* and *P*6_3*mmc*) propotion (Fig. S36). The medium degree of phase fusion successfully increased the high capacity retention from 73 % to 94 % (Fig. 5d-e). Manipulating medium phase fusion in this manner is an effective way to optimize performance, opening up new possibilities for advancing material.

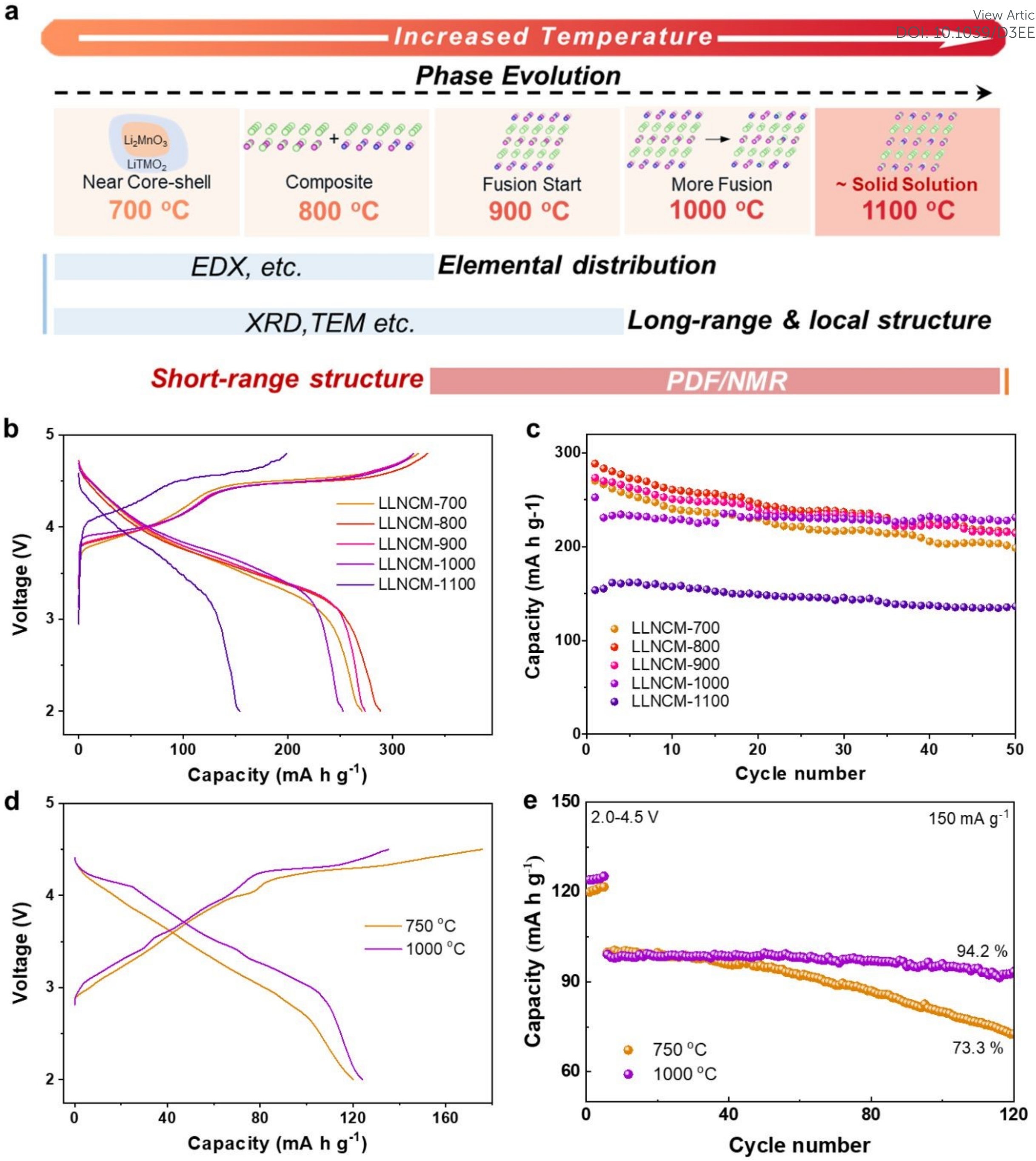

Figure 5. The microscopic picture of phase fusion and the impact on electrochemical performance. (a) Mechanisms and pathways of phase evolution in Li-rich Mn-based cathodes. (b) Capacity-voltage profiles of LLNCM-700, LLNCM-800, LLNCM-900, LLNCM-1000 and LLNCM-1100 cathodes at the first cycle. (c) Cycling performance of different cathodes in the voltage range of 2–4.8 V at 0.1 C. (d) Capacity-voltage profiles of $C2/m$ and $P6_3mmc$ phases calcining at 750 °C and 1000 °C. (e) The corresponding electrochemical performance in the voltage range of 2.0–4.5 V at 1 C after 5 cycles' activation at 0.1 C.

View Article Online
DOI: 10.1039/D3EE04199A

Conclusion

In summary, a thorough investigation was performed on the formation and fusion process of two extremely similar layered phases in Li-rich Mn-based cathode materials from different angles covering elemental distribution, local structure, long-range structure, and short-range structure, by employing a comprehensive multiscale characterization, including TEM EDX, HRTEM, TKD, SXRD, PDF, and ssNMR. It clearly reveals the detailed process from the formation of two phases into different particles, to two-phase merging into individual paticles, eventually to phase fusion within individual particles at the atomic level. Importantly, synchrotron X-ray PDF analysis combined with theoretical simulation demonstrates for the first time that the TM-TM distance increases with the progress of the phase fusion, making it become an effective parameter for judging the extent of phase fusion. Furthermore, the cycling stability was significantly enhanced without sacrificing the capacity by adjusting the phase fusion to a medium extent. This study provides a multiple-technique-integrated methodology to investigate the structural evolution in the complicated multiple-phase system, and also offers valuable insights into the design and optimization of complex layed cathodes by tuning the phase fusion extent.

Experiment Section

Materials preparation

The precursor for $0.5Li[Li_{1/3}Mn_{2/3}]O_2 \bullet 0.5Li[Ni_{1/3}Co_{1/3}Mn_{1/3}]O_2$ (LLNCM) was obtained by a sol-gel method and a subsequent low-temperature sintering. In a typical process, 4.9533 g $CH_3COOLi{\cdot}2H_2O$ (Aladdin, 99 %, 3 % excess), 1.6757 g $(CH_3COO)_2Ni{\cdot}4H_2O$ (Aladdin, 99 %), 4.9513 g $(CH_3COO)_2Mn{\cdot}4H_2O$ (Aladdin, 99 %) and 1.6773 g $(CH_3COO)_2Co{\cdot}4H_2O$ (Aladdin, 99.5%) in the stoichiometric ratio were mixed in 100 mL deionized water. 7.0047 g citric acid and 3.7137 g polyvinylpyrrolidone (Aladdin, K30) were added as the chelating agents. The solution was dried at 95 °C, and then the powder was calcined at 140 °C for 3 hours and 500 °C for 3 hours to obtain the precursor. The precursor was calcined at 700, 800, 900, 1000, and 1100 °C for 20, 15, 12, 10, 6 hours, respectively, to obtain LLNCM-700, LLNCM-800, LLNCM-900, LLNCM-1000 and LLNCM-1100.

View Article Online
DOI: 10.1039/D3EE04199A

Materials characterization

The morphology (Fig. S1) were characterized by scanning electron microscope (SEM, ZEISS Supra 55 field emission scanning electron microscopy). The particle size distribution (Fig. S2) was measured by a Nano-ZS90 zeta potential analyzer . Elemental composition (Table S1) was analyzed using inductively coupled plasma-optical emission spectroscopy (ICP-OES, Model JY2000-2). The HRTEM and SAED images as well as EDX mapping were taken by JEOL-3200FS (FETEM, 300 kV). The atomic structures of the samples were analyzed using high-angle annular dark-field scanning transmission electron microscopy (HAADF-STEM) on a double Cs-corrected FEI Titan Themis G2 TEM, operating at 300 kV. TKD images were collected by FIB (FEI Scios-ZEISS SUPRA® 55) equipped with an Oxford symmetry electron back-scattering diffraction (EBSD) detector. The TKD data was processed by using the Oxford AZtec and HKL CHANNEL 5 software. X-ray powder diffraction and total scattering data of five samples were collected at sector 11-ID-C of the Advanced Photon Source (Argonne National Laboratory). The beam size is 0.5 mm×0.5 mm and the wavelength is 0.1173 Å. *In-situ* heating SXRD measurement at 1000 ℃ was performed at the same beamline. *In-situ* heating XRD measurement at 800 and 900 ℃ was collected by high power Bruker D8-Advance diffractometer using Cu-$K\alpha$ radiation at 50 kV and 100 mA. Rietveld refinement of SXRD patterns and peak fitting were carried out using TOPAS software packages. Rietveld refinement of PDF were performed by PDFgui.[44] TG-DSC was carried out by MDTC-EQ-M05-01. The staking faults was refined by FAULTS program. Two-phase reaction process analyzed by differential scanning calorimetry (DSC, MDTC-EQ-M05-01).[26] The XANES and EXAFS analyses were performed at the BL11B beamline of the Shanghai Synchrotron Radiation Facility (SSRF). MAS NMR spectroscopy were performed on a 400 MHz Bruker ADVANCE III spectrometer at the ^{7}Li Larmor frequency of 155.51 MHz using a triple-resonance 1.9 mm MAS probe. Spectra were recorded using the projected magic-angle turning phase-adjusted sideband separation (pj-MATPASS) pulse sequence with a π/2 pulse length of 1.6 μs and a recycle delay of 50 ms.

Electrochemical tests

Coin-type (CR2032) half cells were assembled to perform the electrochemical measurements. Active materials, polyvinylidene fluoride (PVDF, Solvay® 5130) and carbon black (C45 Conductive Carbon Black, TIMCAL) in the weight ratio of 7:2:1 was mixed in n-methyl-2-pyrrolidone (NMP). The mixture was stirred at 2000 rpm for 9 min (THINKY AR-

100) to form a uniform slurry, which was blade-casted on the Al foil and dried at 80 °C in vacuum for 10 hours. 1.2 M $LiPF_6$ solution in EC / EMC (3:7) mixed solvent was used as the electrolyte. The galvanostatic charge-discharge tests were performed using a NEWARE system battery system (MIHW-200-160CH, 1 C = 200 mA g^{-1}).

Theoretical calculations

All the density functional theory (DFT) calculations were executed in Vienna ab initio Simulation Package (VASP).[45] The Perdew-Burke-Ernzerhof (PBE) form of generalized gradient approximation (GGA) based on projector-augmented wave (PAW) method is selected to describe the electronic exchange-correlation potential.[46-48] The cut-off energy for structural optimization and static electron energy calculation is 520 eV and the electronic energy convergence criterion was set at 10^{-5} eV. The conjugate gradient algorithm is used for ionic relaxation. For correctly characterize the localization of the TM d-electrons, the PEB+U method was used to account for the strong correlation interaction.[49, 50] The short on-site Coulomb interaction (U) presented in the localized 3*d* electrons of Mn, Co and Ni are 4.2, 3.3 and 6.4 eV, respectively. The first Brillouin zone is sampled using the reciprocal grid 2×2×2 of Monkhorst-Pack. The optimized residual force on each atom of Geometries were less than 0.01 eV/Å. DFT-D3 semi-empirical van der waals correction is applied for making up for the defects of DFT in dealing with dispersion force during structural relaxation.[51] The spin-polarized calculations were considered in all our calculations. All calculations were performed considering a ferromagnetic ordering of transition metal atoms. Mn, Ni, and Co are ferromagnetic inside, caculations consider antiferromagnetic between Mn and Ni.[52]

During the phase mixing process, the main source of configuration entropy is the distribution and component of metal ions (Li、Ni、Co、Mn) in transition metal layers. The no-fusion structure composed with Li_2MnO_3 and NMC111 has the well-defined metal distribution. In the theoretically solid solution structure with the maximum degree of mixing, Li^+ and the transition metal ions are randomly arranged. Using the no-fusion structure and solid solution structure as the endmembers, the special quasi-random structure (SQS) models with medium-level and high-level phase fusion (mixing) can be constructed.

Supplementary information

Electronic supplementary information (ESI) available. See DOI:

Acknowledgments

View Article Online
DOI: 10.1039/D3EE04199A

This work was financially supported by the National Natural Science Foundation of China (52172175), the Shenzhen Science and Technology Research Grant (JCYJ20210324130812033), the Shenzhen Key Laboratory of Eco-materials and Renewable Energy (ZDSYS20200922160400001), the Program from Guangdong Introducing Innovative and Entrepreneurial Teams (2019ZT08L101 and RCTDPT-2020-001), the Basic and Applied Basic Research Foundation of Guangdong Province (No. 2021B1515130002) and the Chemistry and Chemical Engineering Guangdong Laboratory (1922018). This research used resources of the Advanced Photon Source, a US Department of Energy (DOE) Office of Science User Facility operated for the DOE Office of Science by Argonne National Laboratory under contract no.DE-AC02-06CH11357.

Author contributions

S.X., F.P.and M.Z conceived the idea and designed the experiments. S.X.and W.R. synthesized all the materials and conducted electrochemical measurements. S.X. designed the phase diagram related experiments. S.X., W.Z. and W.W. carried out the TEM, SAED, HADDF-STEM and TKD measurements. T. L, S.X. performed ex situ synchrotron PDF, XRD and insitu heating XRD. B.H, X.L., H.L., M.Z. and S.X. performed ssNMR and data analysis. S.X., M.Z, C.Y., J.L., X.T., C.D. and F.P. performed structural analysis and refinement. B.Q and S.X carried out the XANES and EXAFS. S.X, X.Y, Z.G., L.W and Z.Y. performed TG-DSC, ICP and SEM characterization. Z.C., C.H. and S.X. conducted DFT calculation. S.X., F.P. and M.Z. wrote the manuscript and all authors edited the manuscript.

Conflicts of interest

There are no conflicts to declare.

View Article Online
DOI: 10.1039/D3EE04199A

Notes and references

1. P. K. Nayak, E. M. Erickson, F. Schipper, T. R. Penki, N. Munichandraiah, P. Adelhelm, H. Sclar, F. Amalraj, B. Markovsky and D. Aurbach, *Adv. Energy Mater.*, 2018, **8**, 1702397.
2. L. Y. Yang, K. Yang, J. X. Zheng, K. Xu, K. Amine and F. Pan, *Chem. Soc. Rev.*, 2020, **49**, 4667–4680.
3. M. H. Rossouw and M. M. Thackeray, *Mater. Res. Bull.*, 1991, **26**, 463–473.
4. F. Ning, B. Li, J. Song, Y. Zuo, H. Shang, Z. Zhao, Z. Yu, W. Chu, K. Zhang, G. Feng, X. Wang and D. Xia, *Nat. Commun.*, 2020, **11**, 4973.
5. A. Singer, M. Zhang, S. Hy, D. Cela, C. Fang, T. A. Wynn, B. Qiu, Y. Xia, Z. Liu, A. Ulvestad, N. Hua, J. Wingert, H. Liu, M. Sprung, A. V. Zozulya, E. Maxey, R. Harder, Y. S. Meng and O. G. Shpyrko, *Nat. Energy*, 2018, **3**, 641–647.
6. Y. Yang, Z. Zhang, S. Liu, B. Wang, J. Liu, Y. Ren, X. Zhang, S. Zhao, D. Liu and H. Yu, *Matter*, 2022, **5**, 3869–3882.
7. F. Amalraj, D. Kovacheva, M. Talianker, L. Zeiri, J. Grinblat, N. Leifer, G. Goobes, B. Markovsky and D. Aurbach, *J. Electrochem. Soc.*, 2010, **157**, A1121.
8. Y. Lei, J. Ni, Z. Hu, Z. Wang, F. Gui, B. Li, P. Ming, C. Zhang, Y. Elias, D. Aurbach and Q. Xiao, *Adv. Energy Mater.*, 2020, **10**, 2002506.
9. A. Boulineau, L. Simonin, J.-F. Colin, E. Canévet, L. Daniel and S. Patoux, *Chem. Mater.*, 2012, **24**, 3558–3566.
10. H. Yu, H. Kim, Y. Wang, P. He, D. Asakura, Y. Nakamura and H. Zhou, *Physical Chemistry Chemical Physics*, 2012, **14**, 6584–6595.
11. J. Bareño, C. H. Lei, J. G. Wen, S.-H. Kang, I. Petrov and D. P. Abraham, *Adv. Mater.*, 2010, **22**, 1122–1127.
12. E. McCalla, A. W. Rowe, J. Camardese and J. R. Dahn, *Chem. Mater.*, 2013, **25**, 2716–2721.
13. Z. Lu and J. R. Dahn, *J. Electrochem. Soc.*, 2002, **149**, A815.
14. Y. Li, S. Xu, W. Zhao, Z. Chen, Z. Chen, S. Li, J. Hu, B. Cao, J. Li, S. Zheng, Z. Chen, T. Zhang, M. Zhang and F. Pan, *Energy Storage Mater.*, 2022, **45**, 422–431.
15. T. Liu, J. Liu, L. Li, L. Yu, J. Diao, T. Zhou, S. Li, A. Dai, W. Zhao, S. Xu, Y. Ren, L. Wang, T. Wu, R. Qi, Y. Xiao, J. Zheng, W. Cha, R. Harder, I. Robinson, J. Wen, J. Lu, F. Pan and K. Amine, *Nature*, 2022, **606**, 305–312.
16. F. Lin, D. Nordlund, T. C. Weng, Y. Zhu, C. Ban, R. M. Richards and H. L. Xin, *Nat. Commun.*, 2014, **5**, 3358.
17. R. Lin, E. Hu, M. Liu, Y. Wang, H. Cheng, J. Wu, J. C. Zheng, Q. Wu, S. Bak, X. Tong, R. Zhang, W. Yang, K. A. Persson, X. Yu, X. Q. Yang and H. L. Xin, *Nat. Commun.*, 2019, **10**, 1650.
18. L. Wang, T. Liu, A. Dai, V. De Andrade, Y. Ren, W. Xu, S. Lee, Q. Zhang, L. Gu, S. Wang, T. Wu, H. Jin and J. Lu, *Nat. Commun.*, 2021, **12**, 5370.
19. N. Guerrini, L. Jin, J. G. Lozano, K. Luo, A. Sobkowiak, K. Tsuruta, F. Massel, L.-C. Duda, M. R. Roberts and P. G. Bruce, *Chem. Mater.*, 2020, **32**, 3733–3740.
20. P. Yan, L. Xiao, J. Zheng, Y. Zhou, Y. He, X. Zu, S. X. Mao, J. Xiao, F. Gao, J.-G. Zhang and C.-M. Wang, *Chem. Mater.*, 2015, **27**, 975–982.
21. T. Matsunaga, H. Komatsu, K. Shimoda, T. Minato, M. Yonemura, T. Kamiyama, S. Kobayashi, T. Kato, T. Hirayama, Y. Ikuhara, H. Arai, Y. Ukyo, Y. Uchimoto and Z. Ogumi, *Chem. Mater.*, 2016, **28**, 4143–4150.
22. X. Liu, G.-L. Xu, V. S. C. Kolluru, C. Zhao, Q. Li, X. Zhou, Y. Liu, L. Yin, Z. Zhuo, A. Daali, J.-J. Fan, W. Liu, Y. Ren, W. Xu, J. Deng, I. Hwang, D. Ren, X. Feng, C. Sun,

L. Huang, T. Zhou, M. Du, Z. Chen, S.-G. Sun, M. K. Y. Chan, W. Yang, M. Ouyang and K. Amine, *Nat. Energy*, 2022, **7**, 808–817.

23. D. Q. Liu, Z. Shadike, R. Q. Lin, K. Qian, H. Li, K. K. Li, S. W. Wang, Q. P. Yu, M. Liu, S. Ganapathy, X. Y. Qin, Q. H. Yang, M. Wagemaker, F. Y. Kang, X. Q. Yang and B. H. Li, *Adv. Mater.*, 2019, **31**, 1806620.
24. X. Wang, Q. Zhang, C. Zhao, H. Li, B. Zhang, G. Zeng, Y. Tang, Z. Huang, I. Hwang, H. Zhang, S. Zhou, Y. Qiu, Y. Xiao, J. Cabana, C.-J. Sun, K. Amine, Y. Sun, Q. Wang, G.-L. Xu, L. Gu, Y. Qiao and S.-G. Sun, *Nat. Energy*, 2024, **9**, 184–196.
25. Y. Tang, Q. Zhang, W. Zuo, S. Zhou, G. Zeng, B. Zhang, H. Zhang, Z. Huang, L. Zheng, J. Xu, W. Yin, Y. Qiu, Y. Xiao, Q. Zhang, T. Zhao, H.-G. Liao, I. Hwang, C.-J. Sun, K. Amine, Q. Wang, Y. Sun, G.-L. Xu, L. Gu, Y. Qiao and S.-G. Sun, *Nat. Sustainability*, 2024, **7**, 348–359.
26. R. Shunmugasundaram, R. S. Arumugam and J. R. Dahn, *J. Electrochem. Soc.*, 2016, **163**, A1394–A1400.
27. B. Li, Z. Zhuo, L. Zhang, A. Iadecola, X. Gao, J. Guo, W. Yang, A. V. Morozov, A. M. Abakumov and J. M. Tarascon, *Nat. Mater.*, 2023, **22**, 1370–1379.
28. Y. He, Y. Zhang, Z. Wang, X. Li, Z. Lü, X. Huang and Z. Liu, *Adv. Funct. Mater.*, 2021, **31**, 2101737.
29. S.-J. Hwang, H.-S. Park, J.-H. Choy and G. Campet, *The Journal of Physical Chemistry B*, 2001, **105**, 335–342.
30. F. Dogan, J. R. Croy, M. Balasubramanian, M. D. Slater, H. Iddir, C. S. Johnson, J. T. Vaughey and B. Key, *J. Electrochem. Soc.*, 2014, **162**, A235–A243.
31. F. Dogan, B. R. Long, J. R. Croy, K. G. Gallagher, H. Iddir, J. T. Russell, M. Balasubramanian and B. Key, *Journal of the American Chemical Society*, 2015, **137**, 2328–2335.
32. X. Liu, Z. Liang, Y. Xiang, M. Lin, Q. Li, Z. Liu, G. Zhong, R. Fu and Y. Yang, *Adv. Mater.*, 2021, **33**, e2005878.
33. O. Pecher, J. Carretero-González, K. J. Griffith and C. P. Grey, *Chem. Mater.*, 2016, **29**, 213–242.
34. Y. Xiang, X. Li, Y. Cheng, X. Sun and Y. Yang, *Mater. Today*, 2020, **36**, 139–157.
35. D. H. Seo, J. Lee, A. Urban, R. Malik, S. Kang and G. Ceder, *Nat. Chem.*, 2016, **8**, 692–697.
36. S. Zhao, K. Yan, J. Zhang, B. Sun and G. Wang, *Angew. Chem. Int. Ed.*, 2021, **60**, 2208–2220.
37. W. Huang, C. Lin, J. Qiu, S. Li, Z. Chen, H. Chen, W. Zhao, G. Ren, X. Li, M. Zhang and F. Pan, *Chem*, 2022, **8**, 2163–2178.
38. Z. Li, Y. Li, M. Zhang, Z. W. Yin, L. Yin, S. Xu, C. Zuo, R. Qi, H. Xue, J. Hu, B. Cao, M. Chu, W. Zhao, Y. Ren, L. Xie, G. Ren and F. Pan, *Adv. Energy Mater.*, 2021, **11**, 2101962.
39. S. Xu, X. Tan, W. Ding, W. Ren, Q. Zhao, W. Huang, J. Liu, R. Qi, Y. Zhang, J. Yang, C. Zuo, H. Ji, H. Ren, B. Cao, H. Xue, Z. Gao, H. Yi, W. Zhao, Y. Xiao, Q. Zhao, M. Zhang and F. Pan, *Angew. Chem. Int. Ed.*, 2023, **62**, e202218595.
40. X. Wu, H. Liu, X. Lou, F. Geng, J. Li, C. Li and B. Hu, *The Journal of Physical Chemistry Letters*, 2023, **14**, 7711–7717.
41. R. A. House, G. J. Rees, M. A. Pérez-Osorio, J.-J. Marie, E. Boivin, A. W. Robertson, A. Nag, M. Garcia-Fernandez, K.-J. Zhou and P. G. Bruce, *Nat. Energy*, 2020, **5**, 777–785.
42. R. A. House, H. Y. Playford, R. I. Smith, J. Holter, I. Griffiths, K.-J. Zhou and P. G. Bruce, *Energy Environ. Sci.*, 2022, **15**, 376–383.

View Article Online
DOI: 10.1039/D3EE04199A

43. P. M. Csernica, S. S. Kalirai, W. E. Gent, K. Lim, Y.-S. Yu, Y. Liu, S.-J. Ahn, E. Kaeli, X. Xu, K. H. Stone, A. F. Marshall, R. Sinclair, D. A. Shapiro, M. F. Toney and W. C. Chueh, *Nat. Energy*, 2021, **6**, 642–652.
44. C. Farrow, P. Juhas, J. Liu, D. Bryndin, E. Božin, J. Bloch, T. Proffen and S. Billinge, *J. Phys.: Condens. Matter*, 2007, **19**, 335219.
45. G. Kresse and J. Hafner, *Phys. Rev. B*, 1993, **47**, 558–561.
46. G. Kresse and D. Joubert, *Phys. Rev. B*, 1999, **59**, 1758–1775.
47. P. E. Blöchl, *Phys. Rev. B*, 1994, **50**, 17953–17979.
48. J. P. Perdew, K. Burke and M. Ernzerhof, *Phys. Rev. Lett.*, 1996, **77**, 3865–3868.
49. S. L. Dudarev, G. A. Botton, S. Y. Savrasov, C. J. Humphreys and A. P. Sutton, *Phys. Rev. B*, 1998, **57**, 1505–1509.
50. V. I. Anisimov, J. Zaanen and O. K. Andersen, *Phys. Rev. B*, 1991, **44**, 943–954.
51. S. Grimme, J. Antony, S. Ehrlich and H. Krieg, *The Journal of Chemical Physics*, 2010, **132**, 154104.
52. S. Q. Wu, Z. Z. Zhu, Y. Yang and Z. F. Hou, *Comput. Mater. Sci*, 2009, **44**, 1243–1251.